Nuclear Materials and Energy 25 (2020) 100797

Contents lists available at ScienceDirect

Nuclear Materials and Energy

journal homepage: www.elsevier.com/locate/nme

Carbonaceous deposits on aluminide coatings in tritium-producing assemblies

Weilin Jiang [a,*], Steven R. Spurgeon [a], Bethany E. Matthews [a], Anil K. Battu [a], Swarup China [a], Tamas Varga [a], Arun Devaraj [a], Elizabeth J. Kautz [a], Matthew A. Marcus [b], Dallas D. Reilly [a], Walter G. Luscher [a]

[a] Pacific Northwest National Laboratory, Richland, WA 99352, USA
[b] Advanced Light Source, Lawrence Berkeley National Laboratory, Berkeley, CA 94720, USA

ARTICLE INFO

Keywords:
Carbonaceous deposit
Iron aluminide coating
TPBAR
Neutron irradiation

ABSTRACT

Co-deposition of carbon atoms with hydrogen isotopes and hydrogenated carbon radicals and molecules is recognized as the main mechanism for tritium retention in the graphite walls of the previous tokamak fusion devices. Significant tritium retention would be a serious concern for safe and economic long-term operation of future fusion test reactors and fusion energy systems. Similar deposits are observed on the surface of the engineered components in a tritium-producing assembly, known as a Tritium-Producing Burnable Absorber Rod (TPBAR). Characterization of the deposits can help understand the tritium transport, accumulation history and distribution in TPBARs. This study reports our recent results from the carbonaceous deposits formed on an aluminide-coated cladding in the lower plenum of a TPBAR following thermal neutron irradiation. The observed deposits are amorphous in nature, consisting of flakes of interconnected nanoscale features. They contain primarily double-bonded carbon (e.g., alkene) and carbonyl carbon, as well as a minor fraction of aliphatic carbon, all of which are likely tritiated. A similar co-deposition process that occurred in previous fusion devices is responsible for the formation and growth of the carbonaceous deposits.

1. Introduction

Deposition of carbon and other elements or chemical species onto plasma facing components (PFCs) has been investigated extensively in Tokamak Fusion Test Reactor (TFTR) [1,2], Joint European Torus (JET) [3–8], Tokamak Experiment for Technology Oriented Research (Textor) [9–12], Experimental Advanced Superconducting Tokamak (EAST) [13,14], Tungsten (W) Environment in Steady-state Tokamak (WEST, formerly Tore Supra) [15–17], and Axially Symmetric Divertor Experiment (ASDEX) [18]. A comprehensive summary of the results from previous studies has been reported [19]. Nuclear grade graphite was used as the material for the PFCs in previous deuterium–tritium (DT) fusion devices partly because of its excellent thermal properties, including no surface melting if accidentally overheated and an extremely high sublimation temperature of ~4000 K [20]. However, physical sputtering and chemical erosion of graphite create an opportunity for co-deposition of carbon atoms and hydrogenated carbon radicals and molecules in the plasma chamber, resulting in significant tritium retention in the deposits on the PFCs. While physical sputtering is better understood, chemical erosion involves more complex processes. It occurs due to a low energy threshold by forming volatile hydrocarbon molecules or loosely bound hydrocarbon radicals, causing a fast erosion of carbon in the first wall. A review of the physical and chemical processes associated with sputtering, erosion and the formation of hydrogenic carbon deposits has been reported [21]. The ability of carbon to trap hydrogenic species in co-deposited layers is well recognized. A very high fraction of up to 51% of the tritium supplied to the plasma was retained around the divertor of DT fusion devices [22,23]. The co-deposition of carbon atoms with hydrogen isotopes as well as the deposition of hydrogenated carbon radicals and molecules is a dominant process for tritium retention in the fusion devices [19]. The thickness of the deposit layer continuously increases with time, leading to fast accumulation of radioactive tritium to an unacceptable level [24]. Significant tritium retention would be a serious concern for the safe and economic long-term operation of future fusion test reactors and fusion energy systems [19]. In order to reduce tritium retention, tungsten has

* Corresponding author.
E-mail address: Weilin.Jiang@pnnl.gov (W. Jiang).

https://doi.org/10.1016/j.nme.2020.100797
Received 18 May 2020; Received in revised form 27 July 2020; Accepted 4 September 2020
Available online 11 September 2020

been selected to replace graphite as the first-wall material for the International Thermonuclear Experimental Reactor (ITER) [24,25].

Similar to a tritium breeder material in a controlled DT fusion device, γ-$LiAlO_2$ pellets in tritium-producing assemblies, commonly known as Tritium-Producing Burnable Absorber Rods (TPBARs), have been irradiated with thermal neutrons [26] under a tritium science program [27]. No TPBAR components were made of graphite or materials with carbon as a major element in the composition. However, there are low-level carbon impurities and surface-absorbed carbon species (i.e., adventitious carbon) in the as-assembled TPBARs. Dark-colored carbonaceous deposits have been observed on the irradiated TBBAR components, including the aluminide coatings on stainless steel cladding. The characteristics of the deposits may provide critical information about how tritium in the gas phase is transported and accumulated within the TPBAR. A technical basis through material characterization is needed to improve our fundamental understanding of the tritium transport and accumulation. This study reports on the phenomena and characterization results of the carbonaceous deposits on the aluminide coatings in a neutron irradiated TPBAR.

2. Experimental details

A TPBAR [28] consists of a series of concentric components as presented in Fig. 1. A stack of annular lithium aluminate (γ-$LiAlO_2$) pellets enriched in ^{6}Li are supported by Zircaloy-4 liner. Thermal neutron irradiation of TPBARs at ~573 K was performed to a total fluence of ~2 × 10^{22} n/cm^2 at the Watts Bar light water reactor for a total of 487.5 effective full power days (EFPD) [26]. Tritium is produced in the pellets due to nuclear reaction ^{6}Li (n, ^{4}He) ^{3}H. While a fraction of tritium atoms were trapped in the pellets, the rest diffused out and released. Most of the released tritium species were absorbed and immobilized by the adjacent nickel-plated Zircaloy-4 getter by forming solid-state tritiated zirconium compounds (hydrides) [28]. An aluminide coating on the inner diameter of the 316 stainless steel coated cladding provides a tritium diffusion barrier to mitigate tritium permeation. Mechanical gaps exist on both ends of the TPBAR internals, permitting gas communication between the pellet-getter gap and the inner surface of surrounding clad.

After neutron irradiation, TPBARs were sectioned and stored under the ambient conditions for ~4 years, which permitted some decay of activated species but still not enough to handle cladding sections outside of a hot cell [26]. The bottom section of a neutron irradiated aluminide coated cladding exhibiting a carbonaceous deposit was chosen for characterization in this study. Specimens were prepared by further in-cell sectioning irradiated cladding tubes. Secondary electron microscopy (SEM) was performed using JEOL JSM-7600F and FEI Helios DualBeam 660 microscopes operating at 15 kV to improve contrast.

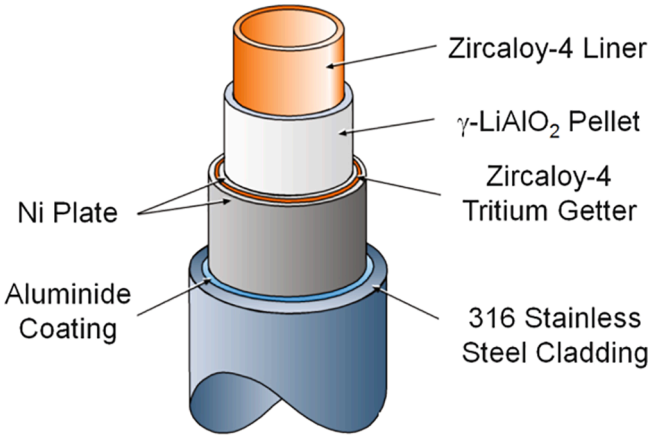

Fig. 1. Schematic representation of a TPBAR [28].

Samples for cross-sectional scanning transmission electron microscopy (STEM) were prepared from the irradiated cladding tube using a Helios 660 focused ion beam (FIB) microscope. A standard lift-out procedure was used, involving Ga^+ ions at 30 keV for cutting/thinning and 2 keV for final polishing. Planar SEM images of the aluminide claddings were taken at 3 kV to improve details of the surface during the FIB process. STEM high-angle annular dark field (STEM-HAADF) imaging was performed using a probe aberration-corrected JEM-ARM 200CF microscope operating at an accelerating voltage of 200 kV with a convergence semi-angle of 27.5 mrad and an inner collection angle of 68 mrad. STEM energy-dispersive X-ray spectroscopy (STEM-EDS) mapping was also performed using a JEOL Centurio detector setup, with a 1 Å probe size, ~120 pA probe current, 10 μs px^{-1} dwell time, and 5–10 min total acquisition time. In addition, convergent beam electron diffraction (CBED) was performed at various locations. Complementary samples from an unirradiated, aluminide coated cladding were also examined to provide a baseline for comparison.

The chemical states of the carbonaceous deposits in the same cross-sectional STEM sample were investigated using scanning transmission X-ray microscopy (STXM) in conjunction with near edge X-ray absorption fine structure (NEXAFS) spectroscopy on beamline 5.3.2.2 at the Advanced Light Source at Lawrence Berkeley National Laboratory in Berkeley, California [29]. To the best of our knowledge, this unique combination of the multimodal approaches represents the first delicate experiment to directly correlate STEM, STXM and NEXAFS characterizations, attempting to reveal the complimentary information of microstructure, composition and chemical states of organic and inorganic components in a radioactive material. The sample was sandwiched between 100 nm thick Si_3N_4 windows before loaded onto a sample holder for the STXM instrument. Experiments were performed using a 25 nm zone plate. Carbon NEXAFS spectra were collected from 278 eV to 320 eV, O spectra from 525 eV to 550 eV, and Fe spectra from 700 to 717 eV (see Supporting Information). The imaging window was 3.5 μm × 2.5 μm. STXM stack images were aligned and processed in MATLAB [30,31]. Relative contributions of chemical groups were quantified through deconvolution of the C K-edge spectra [32]. Self-developed software ("STXM Image Reader" by M.A. Marcus) was used to extract spatially resolved spectra. Following alignment and filtering of the STXM images in the stacks, principal component analysis (PCA) was performed to create cluster maps. Spatially resolved spectra corresponding to these maps were extracted from the data, aligned, pre-edge subtracted, and normalized.

3. Results and discussion

3.1. Unirradiated iron aluminide coating

A half-round tube of unirradiated 316 stainless steel cladding (outer diameter: 9.7 mm) with the inside coated with aluminide is shown in Fig. 2(a). The coating is intended to reduce permeation of tritium through the cladding. The surface of the as-coated aluminide is uneven, showing morphology of aggregated nodules on the surface, as shown in Fig. 2(b). The apparent surface roughness is ~0.6 μm according to the cross-sectional view of the coating layer in Fig. 2(c). There are gaps between the aluminide nodules starting from the surface to a depth of more than 1 μm in some cases. A contrast of major intermetallic phases in the coating is observed, consisting of a ~30 μm thick top layer and a ~50 μm thick buffer layer. This is a result of elemental inter-diffusion at the interface of Al coating and steel substrate at an elevated temperature. The surface aluminide coating consists of two major phases with the top layer containing a major phase of $FeAl_{3.2}$ and the buffer layer mainly of $FeNi_{0.55}Al_{3.7}$ and $FeAl_{2.8}$ [33].

Fig. 3 shows a cross-sectional STEM-HAADF image of an unirradiated aluminide coating. A thin layer is observed on the aluminide surface below the deposited Pt/C protective coating during FIB sample preparation, as shown in Fig. 3(a). Some curtaining is present in the image due

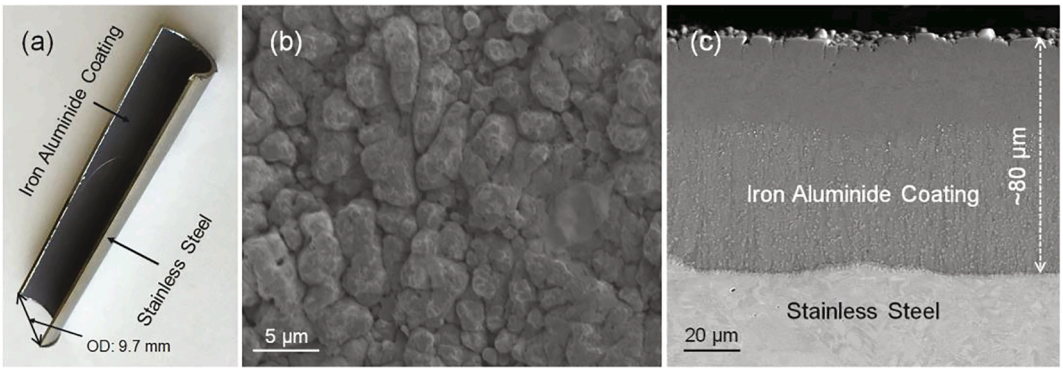

Fig. 2. (a) Photo of a half-round tube of an unirradiated 316 stainless steel cladding coated inside with iron aluminide, and SEM images of the aluminide coating in (b) a planar view and (c) a cross-sectional view. OD: Outer Diameter.

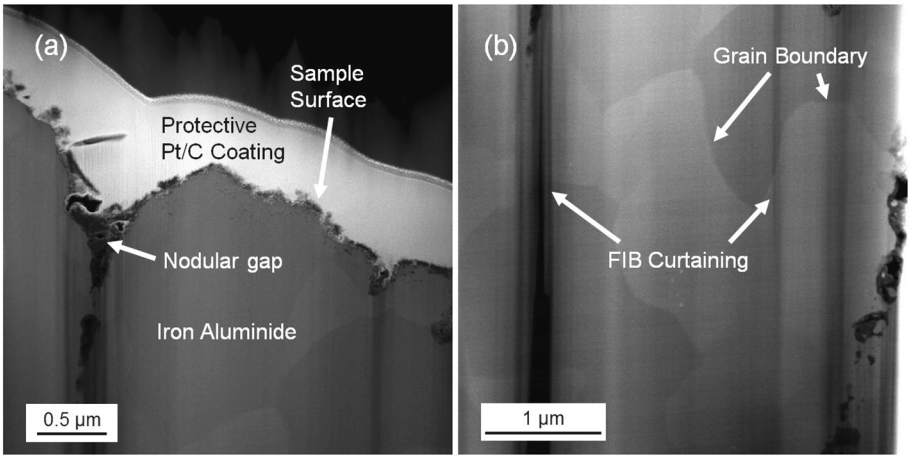

Fig. 3. Cross-sectional STEM-HAADF images of (a) the surface region and (b) the grains in an unirradiated iron aluminide coating.

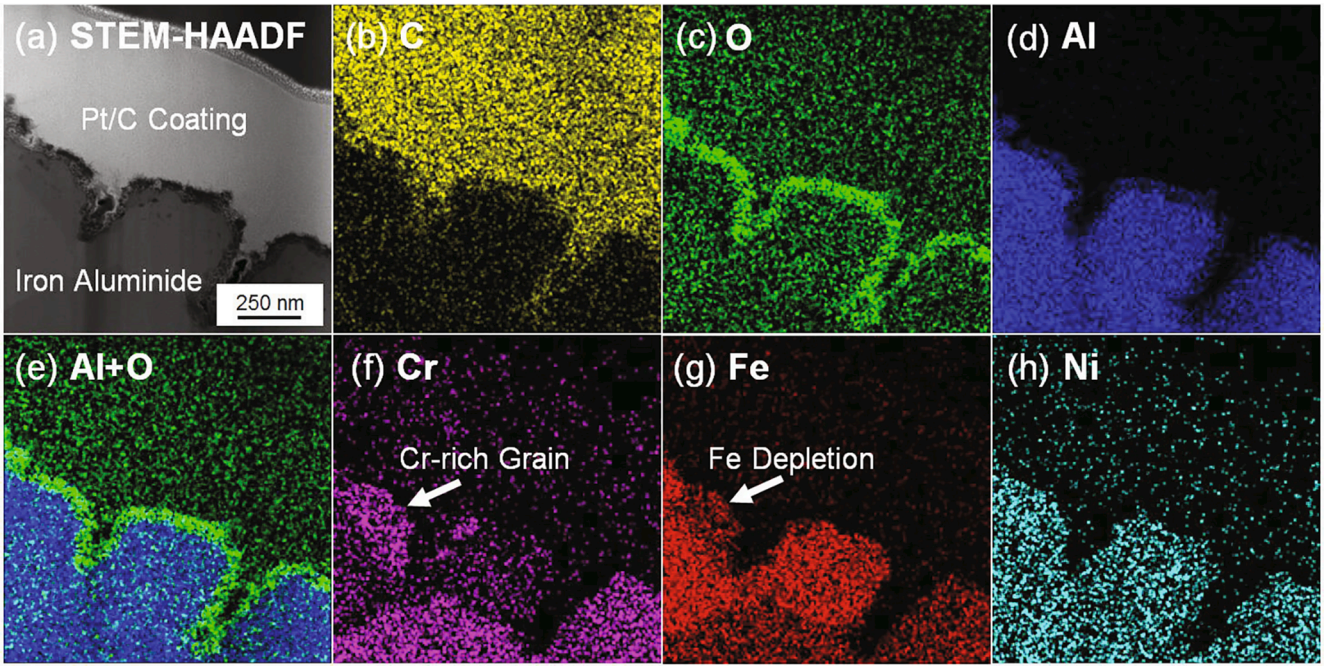

Fig. 4. (a) STEM-HAADF image and STEM-EDS maps of (b) carbon, (c) oxygen, (d) aluminum, (e) combined aluminum and oxygen, (f) chromium, (g) iron, and (h) nickel in the surface region of an unirradiated iron aluminide coating.

to differential ion milling rates during the FIB process. The grain size in the aluminide coating ranges from 0.5 to 1.5 μm, as revealed from Fig. 3 (b). STEM-EDS elemental mapping was performed in selected regions of the unirradiated aluminide coating. Fig. 4 shows typical maps for the elemental distributions of C, O, Al, Al + O, Cr, Fe and Ni. Clearly, there is a ~50 nm thick oxide layer on the aluminide surface that contains primarily Al and some other metallic elements. Carbon is distributed rather uniformly outside the aluminide coating, originating from the deposited surface protective layer of Pt/C, as shown in Fig. 4(a) and 4(b). The combined Al + O map in Fig. 4(e) shows a spatial overlap of the individual elemental maps. Although it is difficult to determine the exact composition of the oxide layer due to its small size in this study, the surface material is likely alumina (Al_2O_3) based on the previous oxidation studies of $FeAl_3$ and FeAl [34,35]. The material will be called aluminum oxide below for convenience. In addition, there is a Cr-rich region with Fe depletion in the aluminide, as shown in Fig. 4(f) and (g).

3.2. Microstructure of carbonaceous deposits

After neutron irradiation, a visible dark-colored layer was observed on some of the TPBAR components. Fig. 5 shows a plan-view SEM image of a neutron irradiated aluminide surface. Compared to Fig. 2(b) for the unirradiated surface, the irradiated material is covered with a layer of flakes and dust. The deposit thickness was observed to depend on the location in the TPBAR. A previous study of similar deposits in TEXTOR tokamak showed that there was no critical thickness at which the deposited layers started to flake and peel off from the surface [12].

In contrast to Fig. 3(a) for the unirradiated aluminide, the irradiated aluminide exhibits a porous network of interconnected nanoscale features on its surface, atop the distinct aluminide oxide layer observed in the unirradiated sample, as shown in Fig. 6. Imaging of the network reveals a complex lacy morphology. The network varies throughout the sample and ranges from 0.1 to 1 μm in the imaged region. The original surface of the deposit in some areas could be removed during the FIB process. The CBED patterns at spots 2 and 3 for nanoscale features show a diffuse intensity, suggesting that the material is amorphous. However, the pattern from spot 1 shows diffraction disks, indicating that the aluminum oxide layer is crystalline.

A region containing the deposit, aluminum oxide layer and aluminide was chosen for elemental mapping, as shown in Fig. 7. Apparently, the layer shows an enhanced carbon intensity [Fig. 7(b)] with the rest of the metallic elements in depletion, confirming that it is a carbonaceous deposit. There also appears to be some oxygen buildup in the deposit region, which is due to the presence of various chemical groups (see section 3.3). Surface oxidation of the FIB samples after exposed to air could enhance the oxygen intensity over the aluminide area [Fig. 7(c)]. H isotopes, He and Li cannot be excluded in the deposit because EDS cannot detect the low atomic number elements. Additionally, Fig. 7(b) reveals a carbon particle at a spot on the coating, which could originate from sample preparation or transfer. The increased intensity along the left side of Fig. 7(b) is a common result of adventitious carbon in the microscope column. This carbon can be polymerized by the beam, accumulating on the sample surface and then fluorescing X-rays during extended STEM-EDS mapping. The particular build-up along the left side of the image is due to the fact that the probe dwelled longer there to account for a "flyback" distortion (hysteresis) during the scanning process, as reported previously [36]. It is interesting to observe that the topmost layer (~20 nm thick) is enriched with O, Fe and Ni with depletion of other metallic elements. There is a thin layer of ~15 nm in thickness between the topmost oxide layer and the aluminide coating, where both O and Al are enriched with Fe and Ni depleted. Thus, this interlayer is mainly composed of aluminum oxide. Similar carbonaceous deposits are observed along the nodular gaps, as shown in Fig. 8, where the aluminum oxide appears to be covered by carbonaceous deposits.

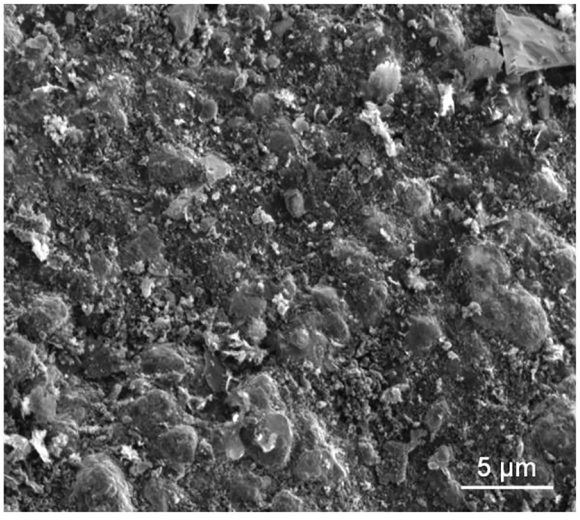

Fig. 5. Plan-view SEM image of neutron irradiated iron aluminide coating surface.

3.3. Chemical states of carbonaceous deposits

The same STEM-EDS sample was used for STXM/NEXAFS to provide complementary chemical states of the carbonaceous deposit. Two different regions were characterized for the NEXAFS at C K-edge, O K-edge, and Fe L_3-edge, as indicated in Fig. 6(a). Fig. 9 shows the representative data obtained from Region 2, while those from Region 1 with similar results are provided in the Supporting Information. Fig. 9(a) shows the optical density of carbon in the imaged region. A higher carbon concentration is observed below the deposit surface (yellow colored). This map shows the difference between post edge (320 eV) and pre-edge (278 eV) absorption, which is representative of the total carbon present. The stack was further analyzed by PCA (4 components) and k-means clustering (3 clusters) [37]. The cluster-average spectra were then used as references to perform a non-negative linear least-squares fit of the spectrum of each pixel, including a sloping background to account for the pre-edge. The loadings of the three cluster spectra are displayed in Fig. 9(b) as red, green and blue intensities. Note that there is a slightly different length scale in Fig. 9(a) and (b)]. Fig. 9(c) shows cluster spectra with dotted lines for the peak energies attributed to different chemical groups with their fractions estimated and plotted in Fig. 9(d). Figures for the deconvolution and fitting of the spectra are shown in Fig. S1 (Supporting Information). It should be noted that the differences between the cluster spectra are not spectacular. The difference at higher energies could be contributed from a differing ratio of non-C to C elements, which would change the ratios of absorption between low and high energies. Saturation effects could also contribute to the difference. The C spectrum shows a large peak at 285.0 eV assigned as aromatic C or C*=C bond (alkenes), as this feature represents an electronic transition from the 1 s state to π* [38–40]. The next major feature, a peak at 286.5 eV, is associated with the C*=O carbonyl group [40] or phenolic C-OH group [41] in ketone compounds. It should be noted that some of the chemical groups presented and discussed below are likely tritiated. The peak around 287.5–287.6 eV may originate from aliphatic C [42]. The feature at 288.3 eV may be associated with amide [43] or possibly O–(C–H)–R groups [41]. C–OH (alcohol) groups are also observed at 289.5 eV. The 291–292 eV portion of the spectrum is attributed to carbonate (CO_3) with a notion that this region is affected by electronic transitions from the C 1 s state to σ*, which includes C–C and C–O bonds [41]. From Fig. 9(c), Cluster 1 in blue is dominated by sp^2 carbon (C*=C), where the inorganic component is concentrated deep below the surface of the deposit on the aluminide [Fig. 9(b)]. The C–H concentration increases gradually from Cluster 1 to the top surface of the deposit (Cluster 2 in green), while the C=O concentration is nearly the same at all depths (in

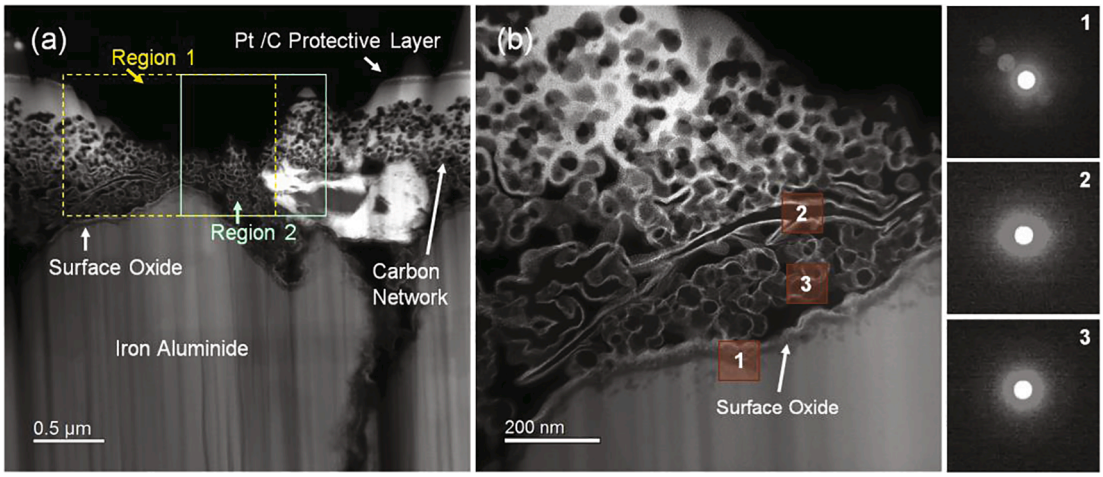

Fig. 6. Cross-sectional STEM-HAADF images of the carbonaceous network on the oxide surface of an irradiated iron aluminide coating at (a) a low- and (b) a higher-resolution. Also included are the CBED patterns from different spots. Regions 1 and 2 are for STXM and EXAFS characterizations.

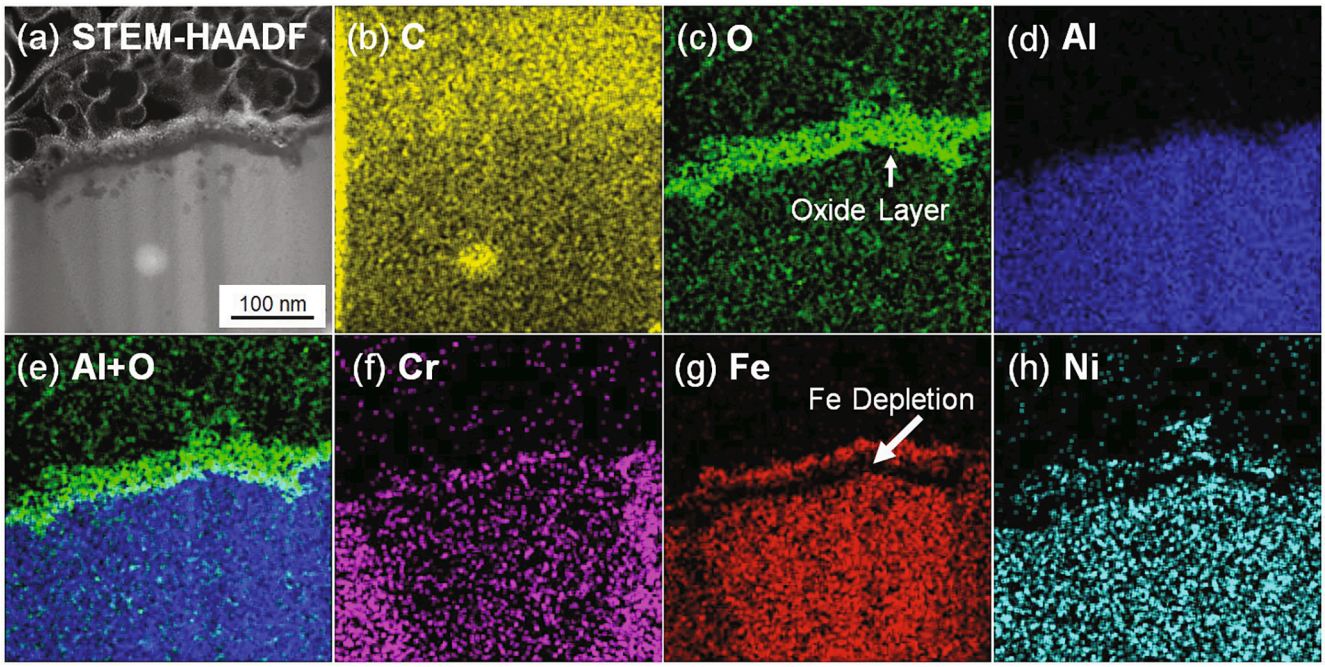

Fig. 7. (a) STEM-HAADF image and STEM-EDS maps of (b) carbon, (c) oxygen, (d) aluminum, (e) combined aluminum and oxygen, (f) chromium, (g) iron, and (h) nickel near the surface of an irradiated aluminide coating.

all the 3 clusters). Overall, STXM and NEXAFS data show that the carbonaceous deposit consists primarily of double-bonded C (e.g., alkene; 35–47%), carbonyl C (26–34%), aliphatic C (5–10%) and alcohol C (2–19%), as summarized in Table 1. The latter two are close to the detection limit, and their percentage values are subject to larger error bars. The carbonate level is below the detection limit. The carbon data in Region 1 is shown in Fig. S2 (Supporting Information), which indicates the presence of the same chemical groups as in Region 2 (Fig. 9).

O K-edge spectra in Fig. S3 (Supporting Information) for Region 1 show a strong pre-edge feature at 531 eV that can be attributed to C=O chemical group (e.g., ketone), while a broad feature observed around 540 eV has been reported to mark the presence of C–O bonds (2 s to σ* transition), which may originate from C–OH (alcohol) or C–O–R (ether) groups [40]. It should be noted that the 531 eV pre-edge feature may also suggest the presence of oxidized Fe, since the feature may originate from transitions of hybridized Fe 3d – O 2p states with t_{2g} and e_g orbital symmetry [44]. The Fe L_3-edge NEXAFS spectra for the same region are shown in Fig. S4 (Supporting Information). A previous study [45] showed that the Fe L_3 absorption spectra for metallic Fe and FeO are very similar, but those for α-Fe_2O_3 and Fe_3O_4 shift slightly to a higher energy level. All the 4 spectra exhibit relatively narrow peaks. The data in Fig. S4 appear to suggest that Cluster 1 with a narrow peak might contain Fe and FeO, where Cr might be rich. Cluster 2 with a broader peak could be resulted from the convolution of the Fe, FeO, Fe_2O_3 and Fe_3O_4 spectra. Although the thin oxide layer on the irradiated aluminide surface is not visible in Fig. S4, the uniform distribution of oxygen across the aluminide area is consistent with the EDS data in Fig. 7(c).

4. Discussion

The Fe and Ni maps in Fig. 7(g) and (h) indicate that the two atomic species in the aluminum oxide layer diffused to the surface during neutron irradiation at ~573 K and Fe became oxidized. However, there

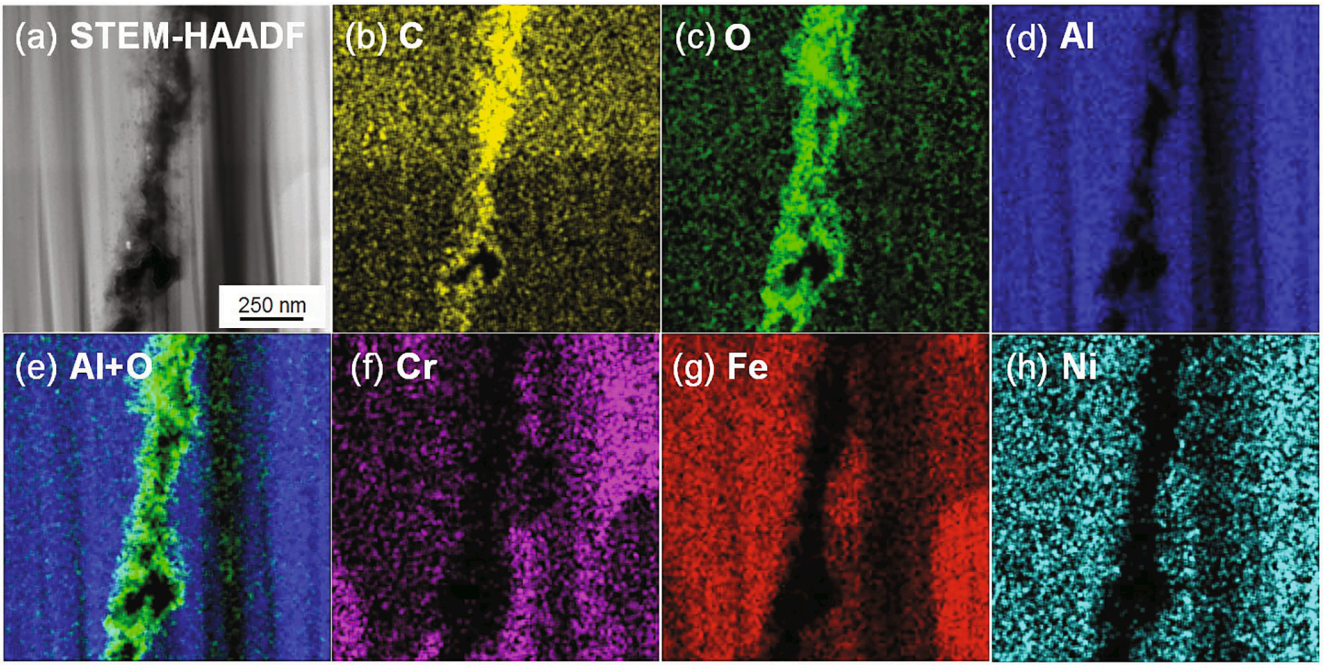

Fig. 8. (a) STEM-HAADF image and STEM-EDS maps of (b) carbon, (c) oxygen, (d) aluminum, (e) combined aluminum and oxygen, (f) chromium, (g) iron, and (h) nickel in a nodular gap in an irradiated aluminide coating.

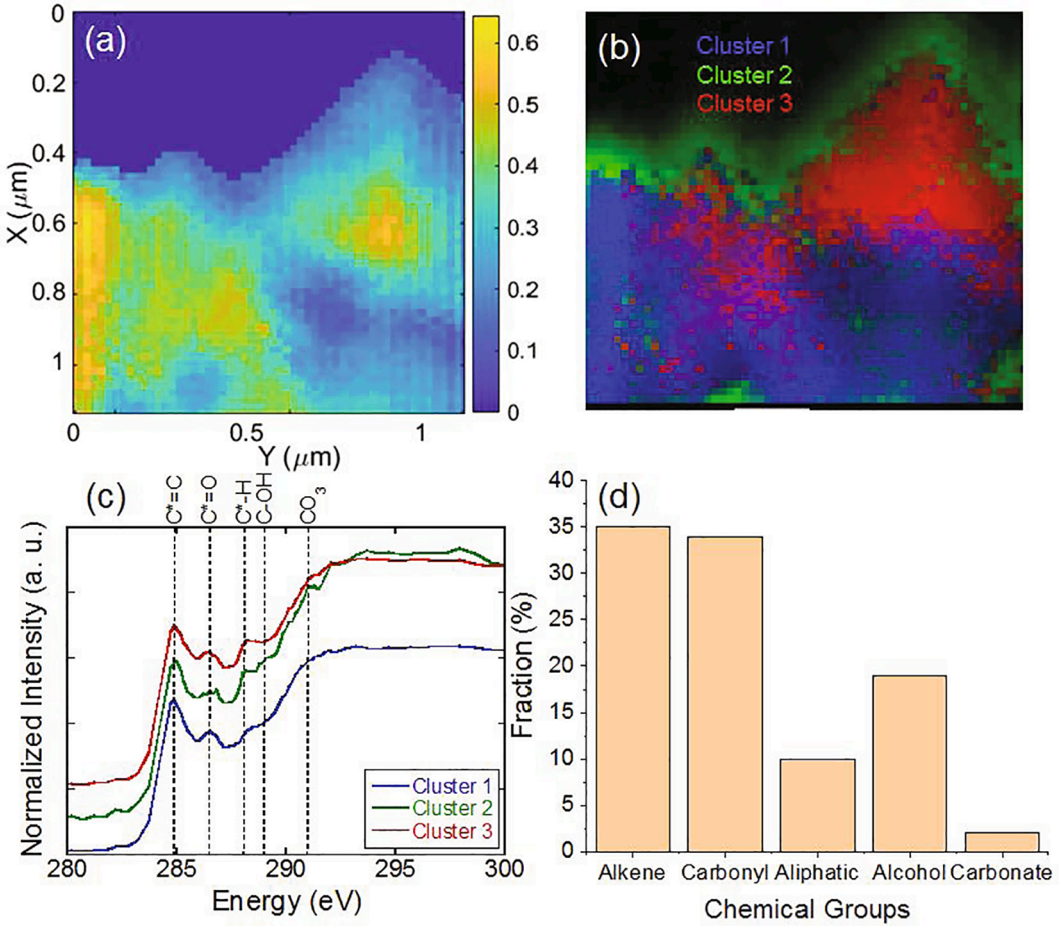

Fig. 9. (a) Optical density map of a carbonaceous deposit, (b) carbon PCA map, (c) NEXAFS spectra with the chemical groups indicated, and (d) fractions of the chemical groups in Region 2 as indicated in Fig. 6(a).

Table 1
NEXAFS peak assignment for various C forms in the carbonaceous deposit.

Energy level (eV)	Carbon form	Fraction (%)	Reference
285.0	aromatic C, C=C bond (e.g., alkene)	35–47	[38–40]
286.5	C=O (e.g., ketone), C–OH (e.g., phenol)	26–34	[40,41]
287.5–287.6	aliphatic C	5–10	[42]
288.3	amide, O(C–H)R, C–OH	2–19	[41,43]
291.0–292.0	CO_3, 1 s to σ* in C–C, C–O	below limit	[41]

is no evidence for carbon atoms in the deposit to diffuse into the surface oxide layer [Fig. 7(b)]. This demonstrates that the surface oxides provide an effective diffusion barrier for carbon. Further studies of hydrogen isotope behavior in the oxide layer are warranted. Aluminum oxide is known to be corrosion resistant [34,35]. The data from this study suggest that aluminum oxide also inhibits reaction between the carbonaceous deposits under the neutron irradiation conditions.

In contrast to previous fusion devices with graphite walls, TPBAR components are not made of graphite or materials with carbon as a major element in the composition. Possible carbon sources in TPBARs include carbon impurities in γ-$LiAlO_2$ pellets during fabrication and sorption of adventitious carbon during storage and assembly of components under ambient conditions. Sorption of CO_2 by $LiAlO_2$ may convert to Li_2CO_3 at elevated temperatures [46]. In contrast to physical sputtering and chemical erosion from the first walls of fusion devices, carbon emission could occur from pellets in TPBARs during neutron irradiation through the thermodynamic process to release the surface-absorbed carbon species (e.g., hydrocarbons) and through the kinetic process (collisions with energetic neutron, helium and tritium particles) to kick out impurity carbon near the pellet surface. In previous fusion devices, co-deposition of carbon atoms and hydrogen isotopes occurred to form a hydrogenated carbon deposit [19]. Chemical erosion could lead to a flux of various C_xQ_y (Q denotes H, D and T) radicals [6,18]. When the radicals hit the component surface, they had a certain probability to stick to it, depending on the sticking coefficients. Radicals were capable of surviving several collisions before finally sticking to a surface and forming a hydrocarbon layer [47]. Similar deposit layers could form in remote areas or inside cavities [7]. Unlike the situation inside a fusion device where H isotopes are abundant, a significant amount of tritium is trapped in pellets and getters, and thus the tritium partial pressure is generally low in TPBARs, especially at the initial stage of TPBAR irradiation. Hydrogen is also present in the TPBAR from ingress through the cladding from the reactor coolant. The cooling water is maintained with an overpressure of hydrogen to minimize corrosion of the TPBAR components during irradiation. The oxygen partial pressure inside the TPBAR is expected to be extremely low.

The data in Fig. 9 generally suggest that C=C population is concentrated below the surface, C=O concentration is nearly constant at all depths, and C–T (C–H) concentration is the highest at the deposit surface and decreases with increasing depth. Outgassing [16] of H isotopes from the carbonaceous deposit may affect their concentrations near the surface, but it is not the primary mechanism during the TPBAR irradiation at 573 K and storage under the ambient conditions. The observed carbon and tritium concentration gradients are likely associated with the lower tritium partial pressure at the initial stage of TPBAR irradiation because tritium release from pellets increases gradually with dose until it reaches a saturation state [27]. The deeper region corresponds to the earlier stage. Similar layers of deposits on PFCs in fusion devices were also observed [9,19,48], revealing the history of carbon and tritium transport during different operation periods. The nearly constant C=O concentration is probably due to a nearly constant partial pressure of oxygen as well as airborne carbon. Hydrocarbon deposit could form as a result of sequential deposition of carbon, tritium and other atoms. Alternatively, C=C and C–T (C–H) radicals and hydrocarbon molecules could form in gaseous phase and then stick to the aluminides. Neither of the two processes may be ruled out in principle, nor should their contributions to the deposit be distinguished. Condensation of hydrogen species in gas phase on the deposit surface after neutron irradiation should also be possible, but this process should not be a dominant one because oxidation of any reactive carbon in the deposit is expected to be favored once the deposit exposed to air. In addition, neither oxidation nor hydrogenation is expected to produce a large H gradient as the carbonaceous deposit is highly porous and very thin in this study.

In parallel, a time-of-flight secondary ion mass spectrometry (ToF-SIMS) study of the same irradiated cladding sample has also been performed, which reveals the presence of both tritium and lithium in the carbonaceous deposit [49]. These light elements either diffused through the nickel plated Zircaloy-4 getter or the mechanical gaps in gaseous phase. Lithium deposition could be independent of carbon. The presence of lithium on the aluminide coating is consistent with our previous ion-irradiation studies [50–52] of γ-$LiAlO_2$ pellets that showed Li evaporation during irradiation at 573 K. It still remains to be investigated how extensively tritium and lithium can permeate the nickel plated Zircaloy-4 getter and whether they can reach the aluminide coating under the irradiation conditions. The results from this study may provide a useful reference about the possible formation of carbonaceous deposits on the first walls of the future fusion devices, reactors or energy systems that have carbon impurities or contamination on the first-wall components.

5. Conclusions

Carbonaceous deposits on aluminide-coated stainless steel cladding in a neutron irradiated TPBAR have been characterized using a multi-modal approach of SEM, STEM, STEM-EDS, CBED, STXM and NEXAFS to characterize the same radioactive sample. An unirradiated aluminide has also been analyzed for comparison. It is observed that Fe and Ni diffused in aluminum oxide during thermal neutron irradiation at ~573 K and Fe became oxidized on the topmost surface. Flaking of carbonaceous deposits is found on the oxide surface. The thickness of the deposits varies with location in the TPBAR. The deposits are amorphous in nature, consisting of interconnected nanoscale features. Similar carbonaceous deposits also appear in the nodular gaps of the aluminide coatings. The deposit contains various chemical groups, including alkene carbon, carbonyl carbon, aliphatic carbon and alcohol carbon, all of which are likely tritiated. Co-deposition of carbon atoms with hydrogen isotopes and hydrogenated carbon radicals and molecules is responsible for the formation of the deposits. The results from this study may help better understand the tritium transport, accumulation and distribution within TPBARs as well as the formation of carbonaceous deposits. The results may also provide a useful reference about possible formation of carbonaceous deposit in future fusion devices, reactors or energy systems.

CRediT authorship contribution statement

Weilin Jiang: Methodology, Formal analysis, Writing - original draft, Supervision. **Steven R. Spurgeon:** Investigation, Formal analysis, Writing - review & editing. **Bethany E. Matthews:** Investigation, Writing - review & editing. **Anil K. Battu:** Investigation, Formal analysis. **Swarup China:** Investigation, Formal analysis. **Tamas Varga:** Investigation, Formal analysis, Writing - original draft. **Arun Devaraj:** Methodology, Writing - review & editing. **Elizabeth J. Kautz:** Investigation, Writing - review & editing. **Matthew A. Marcus:** Resources, Writing - review & editing. **Dallas D. Reilly:** Resources, Investigation. **Walter G. Luscher:** Conceptualization, Writing - review & editing, Project administration, Funding acquisition.

Declaration of Competing Interest

The authors declare that they have no known competing financial interests or personal relationships that could have appeared to influence the work reported in this paper.

Acknowledgements

This research is a part of the Nuclear Process Science Initiative at the Pacific Northwest National Laboratory. It was conducted under the Laboratory Directed Research and Development Program at PNNL, a multi-program national laboratory operated by Battelle for the U.S. Department of Energy under Contract DE-AC05-76RL01830. TEM sample preparation was performed in the Radiological Microscopy Suite, located in the Radiochemical Processing Laboratory (RPL) at PNNL. STXM/NEXAFS analysis at beamline 5.3.2.2 of the Advanced Light Source at Lawrence Berkeley National Laboratory is supported by the Director, Office of Science, Office of Basic Energy Sciences of the U.S. Department of Energy. The authors are grateful to David Senor for informative and stimulating discussions and to Sayan Chatterjee for his effort on the initial sample assessment.

Appendix A. Supplementary data

Supplementary data to this article can be found online at https://doi.org/10.1016/j.nme.2020.100797.

References

[1] B.E. Mills, D.A. Buchenauer, A.E. Pontau, M. Ulrickson, J. Nucl. Mater. 162–164 (1989) 343.
[2] C.H. Skinner, C.A. Gentile, M.M. Menon, R.E. Barry, Nucl. Fusion 39 (1999) 1081.
[3] J.P. Coad, M. Rubel, J. Likonen, N. Bekris, S. Brezinsek, G.F. Matthews, M. Mayer, A.M. Widdowson, JET contributors, Fusion Eng. Des. 138 (2019) 78.
[4] R. Behrisch, J. Ehrenberg, M. Wielunski, A.P. Martinelli, H. Bergsåker, B. Emmoth, L. De Kock, J.P. Coad, J. Nucl. Mater. 145–147 (1987) 723.
[5] J. Likonen, S. Lehto, J.P. Coad, T. Renvall, T. Sajavaara, T. Ahlgren, D.E. Hole, G. F. Matthews, J. Keinonen, JET-EFDA contributors, Fusion Eng. Des. 66–68 (2003) 219.
[6] M. Rubel, J.P. Coad, D. Hole, JET-EFDA contributors, Vacuum 78 (2005) 255.
[7] S. Krat, Y.u. Gaspayan, A. Pisarev, M. Mayer, U. von Toussaint, P. Coad, A. Widdowson, JET-EFDA contributors, J. Nucl. Mater. 463 (2015) 822.
[8] H.G. Esser, V. Philipps, M. Freisinger, A. Widdowson, K. Heinola, A. Kirschner, S. Moller, P. Petersson, S. Brezinsek, A. Huber, G.F. Matthews, M. Rubel, G. Sergienko, JET-EFDA contributors, J. Nucl. Mater. 463 (2015) 796.
[9] A. Weckmann, P. Petersson, M. Rubel, P. Strom, T. Kurki-Suonio, K. Sarkimaki, A. Kirschner, A. Kreter, S. Brezinsek, J. Romazanov, P. Wienhold, A. Pospieszczyk, A. Hakola, M. Airila, Nucl. Mater. Eng. 17 (2018) 83.
[10] M. Rubel, P. Wienhold, D. Hildebrandt, J. Nucl. Mater. 290–293 (2001) 473.
[11] V. Philipps, P. Wienhold, A. Kirschner, M. Rubel, Vacuum 67 (2002) 399.
[12] M. Rubel, V. Philipps, T. Tanabe, P. Wienhold, M. Freisinger, J. Linke, J. von Seggren, E. Wessel, Physica Scripta T81 (1999) 7.
[13] W.R. Wampler, R.A. Pitts, S. Carpentier-Chouchana, P.C. Stangeby, F. Ding, H. M. Mao, W.Z. Wang, J.P. Qian, X. Gong, G.-N. Luo, Phys. Scr. T159 (2014) 014069.
[14] Q. Xu, Z. Yang, G.-N. Luo, Jpn. J. Appl. Phys. 54 (2015) 096201.
[15] S. Panayotis, B. Pégourié, E. Caprin, D. Douai, J.-C. Hatchressian, V. Negrier, J.-Y. Pascal, S. Vartanian, J. Bucalossi, P. Monier-Garbet, J. Nucl. Mater. 438 (2013) S1059.
[16] B. Pegourie, S. Panayotis, P. Languille, C. Martin, T. Dittmar, E. Gauthier, J.-C. Hatchressian, J.-Y. Pascal, P. Roubin, R. Ruffe, E. Tsitrone, S. Vartanian, H. Wanga, A. Beaute, J. Bouvet, C. Brosset, J. Bucalossi, M. Cabie, E. Caprin, X. Courtois, R. Dachicourt, E. Delchambre, C. Dominici, D. Douai, A. Ekedahl, J. P. Gunn, A. Hakola, W. Jacob, H. Khodja, J. Likonen, F. Linez, A. Litnovsky, Y. Marandet, S. Markelj, A. Martinez, M. Mayer, O. Meyer, P. Monier-Garbet, P. Moreau, V. Negrier, P. Oddon, C. Pardanaud, B. Pasquet, P. Pelicon, P. Petersson, V. Philipps, G. Possnert, D. Reiter, J. Roth, I. Roure, M. Rubel, F. Saint-Laurent, F. Samaille, P. Vavpetič, J. Nucl. Mater. 438 (2013) S120.
[17] C. Pardanaud, C. Martin, G. Giacometti, N. Mellet, B. Pégourié, P. Roubin, Thin Solid Films 581 (2015) 92.
[18] V. Rohde, M. Mayer, the ASDEX Upgrade Team, Physica Scripta T103 (2003) 25.
[19] G. Federici, C.H. Skinner, J.N. Brooks, J.P. Coad, C. Grisolia, A.A. Haasz, A. Hassanein, V. Philipps, C.S. Picher, J. Roth, W.R. Wampler, D.G. Whyte, Nucl. Fusion 41 (2001) 1967.
[20] J. Abrahamson, Carbon 12 (1974) 111.
[21] W. Jacob, Thin Solid Films 326 (1998) 1.
[22] C.H. Skinner, W. Blanchard, J. Kamperschroer, P. LaMarche, D. Mueller, A. Nagy, S. Scott, G. Ascione, E. Amarescu, R. Camp, M. Casey, J. Vac. Sci. Technol. A 14 (1996) 3267.
[23] C.H. Skinner, E. Amarescu, G. Ascione, E. Synakowski, J. Nucl. Mater. 241–243 (1997) 214.
[24] H. Bolt, V. Barabash, G. Federici, J. Linke, A. Loarte, J. Roth, K. Sato, J. Nucl. Mater. 307–11 (2002) 43.
[25] Technical Basis for the ITER Final Design Report, Cost Review and Safety Analysis (FDR), ITER EDA Documentation Series No. 16, IAEA, Vienna, 1998.
[26] D.E. Burkes, Cycle 13 TPBAR PIE Plan, PNNL-TTP-8-003, Revision 0, Jan. 17, 2017.
[27] D.J. Senor, Recommendations for Tritium Science and Technology Research and Development in Support of the Tritium Readiness Campaign, PNNL-22873e1, Revision 1, Nov. 7, 2014.
[28] K.A. Burns, E.F. Love, C.K. Thornhill, Description of the tritium-producing burnable absorber rod for the commercial light water reactor, PNNL-22086, February 2012.
[29] T. Warwick, H. Ade, D. Kilcoyne, M. Kritscher, T. Tylisczcak, S. Fakra, A. Hitchcock, P. Hitchcock, H. Padmore, J. Synchrotron Rad. 9 (2002) 254.
[30] B. Wang, T.H. Harder, S.T. Kelly, D.S. Piens, S. China, L. Kovarik, M. Keiluweit, B. W. Arey, M.K. Gilles, A. Laskin, Nat. Geosci. 9 (2006) 433.
[31] R.C. Moffet, A.V. Tivanski, M.K. Gilles, Fundamentals and Applications in Aerosol Spectroscopy, eds. R. Signorell and J.P. Reid, CRC Press, 2010.
[32] D.Q. Pham, R. O'Brien, M. Fraund, D. Bonanno, O. Laskina, C. Beall, K.A. Moore, S. Forestieri, X. Wang, C. Lee, C. Sultana, V. Grassian, C.D. Cappa, K.A. Prather, R. C. Moffet, ACS Earth Space Chem. 1 (2017) 551.
[33] B. Johnson, N. L. Canfield, B. E. Matthews, J. Silverstein, private communications.
[34] P.F. Tortorelli, K. Natesan, Mater. Sci. Eng. A 258 (1998) 115.
[35] N.S. Stoloff, Mater. Sci. Eng. A 258 (1998) 1.
[36] X. Sang, A.R. Lupini, R.R. Unocic, M. Chi, A.Y. Borisevich, S.V. Kalinin, E. Endeve, R.K. Archibald, S. Jesse, Adv. Struct. Chem. Imag. 2 (2016) 6.
[37] M. Lerotic, C. Jacobsen, T. Schäfer, S. Vogt, Ultramicroscopy 100 (2004) 35.
[38] C. Chen, J. Dynes, J. Wang, C. Karunakaran, D.L. Sparks, Environ. Sci. Technol. 48 (2014) 6678.
[39] Y.K. Henneberry, T.E.C. Kraus, P.S. Nico, W.R. Horwath, Org. Geochem. 48 (2012) 81.
[40] M. Uesugi, M. Ito, H. Yabuta, H. Naraoika, F. Kitajima, Y. Takano, H. Mita, Y. Kebukawa, A. Nakato, Y. Karouji, Meteor. Planet. Sci. 54 (2019) 638.
[41] M. Harano, R. Murao, Nippon Steel & Sumitomo Metal Technical Report, No. 118, March 2018; https://www.nipponsteel.com/en/tech/report/nssmc/pdf/118-15.pdf.
[42] J. Lehmann, B. Liang, D. Solomon, M. Lerotic, F. Luizao, J. Kinyangi, T. Schafer, S. Wirick, C. Jacobsen, Global Biogeochem. Cycles 19 (2005) 1.
[43] A.C. Cismasu, F.M. Michel, A.S.P. Tcaciuc, T. Tyliszczak, J. Brown, E. Gordon, G. E. Brown Jr., Comptes Rendus Geosci. 343 (2011) 210.
[44] S. Lafuerza, G. Subias, J. Garcia, S. Di Matteo, J. Blasco, V. Cuartero, C.R. Natoli, J. Phys. Cond. Matter. 23 (2011) 325601.
[45] T.J. Regan, H. Ohldag, C. Stamm, F. Nolting, J. Lüning, J. Stöhr, R.L. White, Phys. Rev. B 64 (2001) 214422.
[46] T. Ávalos-Rendón, J. Casa-Madrid, H. Pfeiffer, J. Chem. A 113 (2009) 6919.
[47] A. von Keudell, C. Hopf, T. Schwarz-Selinger, W. Jacob, Nucl. Fusion 39 (1999) 1451.
[48] M. Rubel, V. Philipps, T. Tanabe, P. Wienhold, M. Freisinger, J. Linke, J. von Seggern, E. Wessel, Physica Scripta T103 (2003) 20.
[49] X.Y. Yu, et al., to be submitted, 2020.
[50] W. Jiang, S.R. Spurgeon, Z. Zhu, X. Yu, K. Kruska, T. Wang, J. Cigax, L. Shao, D. J. Senor, J. Nucl. Mater. 511 (2018) 1.
[51] W. Jiang, J. Zhang, D.J. Edwards, N.R. Overman, Z. Zhu, L. Price, J. Gigax, E. Castanon, L. Shao, D.J. Senor, J. Nucl. Mater. 494 (2017) 411.
[52] W. Jiang, J. Zhang, L. Kovarik, Z. Zhu, L. Price, J. Gigax, E. Castanon, X. Wang, L. Shao, D.J. Senor, J. Nucl. Mater. 484 (2017) 374.